Tuning of the Berry curvature in 2D perovskite polaritons

Laura Polimeno, Milena de Giorgi, Giovanni Lerario, Luisa de Marco, Lorenzo Dominici, Francesco Todisco, Vincenzo Ardizzone, Marco Pugliese, Annalisa Coriolano, Carmela T Prontera, et al.

Tuning of the Berry curvature in 2D perovskite polaritons

Laura Polimeno[1,2,3], Giovanni Lerario[2], Milena De Giorgi[2*], Luisa De Marco[2***], Lorenzo Dominici[2], Francesco Todisco[2], Annalisa Coriolano[1,2], Vincenzo Ardizzone[2], Marco Pugliese[1,2], Carmela T. Prontera[2], Vincenzo Maiorano[2], Anna Moliterni[4], Cinzia Giannini[4], Vincent Olieric[5], Giuseppe Gigli[1,2], Dario Ballarini[2], Qihua Xiong[6], Antonio Fieramosca[6], Dmitry D. Solnyshkov[7,8 **], Guillaume Malpuech[7], Daniele Sanvitto[2,3]

[1]Dipartimento di Matematica e Fisica, "Ennio de Giorgi", Università Del Salento, Campus Ecotekne, via Monteroni, Lecce, 73100, Italy.

[2]CNR NANOTEC, Institute of Nanotechnology, Via Monteroni, 73100 Lecce, Italy.

[3] INFN Istituto Nazionale di Fisica Nucleare, Sezione di Lecce, 73100 Lecce, Italy.

[4]Istituto di Cristallografia, CNR, Via Amendola, 122/O Bari, 70126 Italy.

[5]Paul Scherrer Institute, Forschungstrasse 111, Villigen-PSI, 5232, Switzerland.

[6]Division of Physics and Applied Physics, School of Physical and Mathematical Sciences, Nanyang Technological University, 637371, Singapore.

[7]Institut Pascal, PHOTON-N2, Université Clermont Auvergne, CNRS, SIGMA Clermont, F-63000 Clermont-Ferrand, France.

[8]Institut Universitaire de France (IUF), 75231 Paris, France.

*Corresponding author : milena.degiorgi@nanotec.cnr.it;

** For theoretical informations : dmitry.solnyshkov@uca.fr;

*** For material informations : luisa.demarco@nanotec.cnr.it;

Abstract

Topological physics and in particular its connection with artificial gauge fields is a forefront topic in different physical systems, ranging from cold atoms to photonics and more recently semiconductor dressed exciton-photon states, called polaritons. Engineering the energy dispersion of polaritons in microcavities through nanofabrication or exploiting the intrinsic material and cavity anisotropies has demonstrated many intriguing effects related to topology and emergent gauge fields such as the anomalous quantum Gall and Rashba effects. Here, we show that we can obtain different Berry curvature distributions of polariton bands in a strongly coupled organic-inorganic 2D perovskite single crystal microcavity. The spatial anisotropy of the perovskite crystal combined with photonic spin-orbit coupling produce two Hamilton's diabolical points in the dispersion. The application of an external magnetic field breaks time reversal symmetry thanks to the exciton Zeeman splitting, which lifts the diabolical points degeneracy. As a result, the bands show non-zero integral Berry curvatures which we directly measure by state tomography. Crucially, we show that in addition to measure the different Berry curvatures of the multimode microcavity dispersions, we can also modify the Berry curvature distribution, the so-called band geometry, within each band by tuning external parameters, such as temperature, magnetic field and sample thickness.

The generation of artificial gauge fields (AGF) is a central topic in modern physics and has been recently investigated in a great variety of physical platforms [1], such as ultra-cold atomic gases [2, 3, 4], photonic crystals [5, 6, 7], graphene and graphene like materials [8, 9], mechanical systems [10] and exciton-polaritons [11, 12, 13]. One of the main concepts behind the theory of AGF in photonic systems lies in the topological and geometrical properties of bands associated to the buildup of a non-zero Berry curvature. The Berry curvature is an AGH [<berry1984>] which behaves as a pseudomagnetic field in the reciprocal space, and it is determined by the wave function change along particle energy dispersion.

The Berry curvature, whose integral is a topological invariant called the Chern number, plays a key role in topological physics. To achieve a non-zero integral value of the Berry curvature for a band in a photonic system, both the optical spin-orbit coupling and the breakdown of the time-reversal symmetry (TRS) are necessary [14]. Indeed, the combination of such geometrically non-trivial bands and a band gap then allows the opening of a topological gap [15, 16].

Recently, the frontiers of this field have been extended to the exciton-polariton systems resulting from the strong coupling of excitons and photons. The importance of the exciton-polaritons [16] lies in the possibility to have a high degree of freedom in the engineering of the particles's Hamiltonian when combining the physical phenomena associated to the exciton component, as the exciton Zeeman effect, with those due to the photon energy dispersion in optical confined systems, in particular, photonic spin-orbit coupling [17]. Several strategies to realize topological systems with polaritons have been suggested [18, 19, 20], by using artificial lattices with honeycomb geometries that have been shown to support Dirac cone dispersions [21, 22], as well as edge modes [23].Recently, artificial lattices have been realized both in organic [24] and perovskite materials [25], paving the way for the realization and control of quantum states stable at room temperature (RT), thanks to the intrinsic robustness of the exciton in these materials.

In this context, polariton systems based on 2D hybrid organic-inorganic perovskites [26, 27, 28, 29, 30] represent a unique platform for topological studies, thanks to the possibility to easily tune the optoelectronic properties of the polariton device [31], without the need of complex fabrication techniques.

In this work, we study the topological properties of an exciton-polariton planar resonator made

of 2D perovskites. The bare photonic modes demonstrate linear birefringence, and, in some cases, emergent optical activity [32, 33]. In particular, we demonstrate that a non-zero integral value of the Berry curvature (B_z) is obtained in presence of an external magnetic field, necessary to break the TRS, making use of the exciton Zeeman splitting. Furthermore, we perform direct measurements of the Berry curvature distribution, the so-called band geometry, at different temperatures from cryogenic up to room temperature. We demonstrate that the band geometry can be controlled through the exciton/photon fractions of the polariton mode, the intensity of an external magnetic field (via Zeeman splitting) and temperature.

Our findings pave the way for the formation of topological states and manipulation of their topological properties in perovskite-based polariton systems, capable of working at room temperature.

I. RESULTS AND DISCUSSION

The 4-fluorophenethylammonium lead iodide ($F-(C_6H_5(CH_2)_2NH_3)_2PbI_4$) perovskite crystals (PEAI-F) were synthesized by anti-solvent vapor assisted crystallization method [34, 31] on the top of a Distributed Bragg Reflector (DBR). Single-crystal X-ray diffraction measurements highlight the in-plane distortion of the inorganic layers with octahedra tilting (Fig. S1, S2 and Table S1-S3 of the Supporting Information (SI)), which could favor the optical birefringence of the material. After mechanical exfoliation performed in order to obtain crystals with thickness between 3 μm and 10 μm, the planar cavities are closed with a silver top mirror (Fig. 1A).

The samples inserted in a cryostat equipped for high magnetic field measurements are non-resonantly excited. Polarization-resolved photoluminescence (PL) is measured at different magnetic field between 0 T and 9 T and at different temperature, from 4 K up to room temperature. Fig. 1B, C shows a typical energy dispersion versus the in-plane momentum, obtained from the photoluminescence spectra as $(I_H - I_V)/(I_H + I_V)$ along opposite k directions at 0 T and 4 K, where I_H and I_V are the PL intensities of the horizontal and vertical polarizations, respectively. A manifold of modes, which come in pairs due to a linear polarization splitting, results from the free spectral range of the microcavity, filled with a 7 μm thick perovskite layer (Fig. 1B, C). Neglecting polarization splitting, the energy of the bare photon modes of the Fabry-Perot resonator at k=0 is given by $E_n \approx j\frac{\hbar\pi c}{Ln_r}$ where j is the mode number, L the effective cavity

thickness, n_r the effective refractive index of the cavity. Here $j \sim 50$ and the flattening of the mode dispersion that we observe while approaching the exciton resonance, at 2.364 eV (Fig. S3B), is due to the strong coupling between the bare exciton of the PEAI-F crystal and the cavity modes, and not to the weak increase of the photon mode effective mass which is proportional to *j* and which is less than 5% on the displayed energy scale. Therefore, the differences in the polariton effective mass between different modes are caused by the increase of the exciton fraction. The energy dispersion of a given exciton-polariton mode, labelled by *j* as photonic modes, can be approximately found by diagonalizing a two by two Hamiltonian, describing two coupled linear oscillators (Section V of the SI). The photon fraction p_j decreases while approaching the exciton energy. In the same way, the polariton's effective mass is $\sim m_j^p / p_j$ where m_j^p is the bare photon mass of the mode j. We now concentrate on a given polarization doublet.

The different energy-momentum dispersion of the two modes in a given pair relates to the TE and TM (Transverse Electric, Transverse Magnetic) polarization anisotropy, resulting in an energy splitting of the polariton modes in the order of few meV, which increases at higher wavevector *k*. Such momentum dependent splitting is due both to the intrinsic asymmetry of the cavity and to the difference between the in- and out-of-plane refractive indexes of the perovskite [35]. In the absence of any other refractive index asymmetry, the splitting should be zero at zero momentum $\{k_x, k_y\} = \{0, 0\}\ \mu m^{-1}$. In the PEAI-F-based sample, the presence of the fluorine at the termination of the interlayer in between the perovskite wells introduces an in-plane optical anisotropy, leading to an additional energy splitting (X-Y splitting) between linearly polarized modes at the $\{k_x, k_y\} = \{0, 0\}\ \mu m^{-1}$ point, shifting the degeneracy points (Hamilton's diabolical points) towards higher wavevectors (Fig. 1B) in one in-plane *k* direction (k_y), while no crossing points are visible in the orthogonal direction (k_x) (Fig. 1C). The birefringence splitting for the lowest observed energy polariton mode is ~ 2 meV, which is about two orders of magnitude higher than the typical energy splitting observed in inorganic GaAs based microcavities (15 − 30 μeV) [14, 36]. This value decreases when the photon fraction decreases (Fig. S4C) due to the flattening of the dispersions at the exciton resonance. Another pure optical contribution is an emergent optical activity (OA), similar to that reported in refs. [32] and [33], which arises when modes of different parities couple and anti-cross, giving rise to circularly-polarized contributions even in the

absence of an applied magnetic field. Contrary to the Zeeman splitting, the OA contribution depends on the sample thickness, i.e. it increases when increasing the thickness of the material.

An effective two-band Hamiltonian describing a pair of polariton bands and accounting for the TE-TM, birefringence, Zeeman splitting and OA [32, 33] reads:

$$H_K = \left(E_0 + \frac{\hbar^2 k^2}{2m}\right) I + \begin{pmatrix} \Delta_z + \zeta \mathbf{k}\mathbf{u}_\zeta & \alpha e^{i\varphi_\alpha} - \beta\, k^2\, e^{-2i\varphi_k} \\ \alpha e^{-i\varphi_\alpha} - \beta\, k^2\, e^{+2i\varphi_k} & -\Delta_z - \zeta \mathbf{k}\mathbf{u}_\zeta \end{pmatrix} \quad (1)$$

where *I* is the identity matrix, E_0 the energy of the considered polariton mode at k=0, m the polariton mass, k = |k| = $\sqrt{k_x^2 + k_y^2}$ is the in-plane wavevector module and φ_k its polar angle, Δ_z is the polariton Zeeman splitting, α, β and ζ are the strengths of the X-Y, TE-TM splitting and OA, respectively. φ_α describes the orientation of the linearly polarized eigenmodes at *k*=0 (linear birefringence). $\mathbf{u}_\zeta$ is a unitary vector related to the orientation of the OA. For φ_α= 0 and $\mathbf{u}_\zeta$ oriented along *x*, the system's eigenvalues are obtained by diagonalizing the Hamiltonian in (1):

$$E_\pm = E_0 + \frac{\hbar^2 k^2}{2m} \pm \sqrt{\beta^2 k^4 - \beta\, \alpha\, k^2 \cos(2\varphi_k) + \frac{\alpha^2}{4} + (\Delta_z + \zeta k \cos\varphi_k)^2} \quad (2)$$

The dashed blue and red lines in Figs. 1B, C represent the energy eigenvalues of the system for a pair of orthogonally polarized polariton modes using formula (2). The OA contribution is negligible in the fitting of the energy dispersion because the resulting energy splitting (~ 0.1 meV) is small compared to the full width at half maximum of the modes (~ 1.5 meV). By comparing the dispersion spectra along the two directions, it can also be observed the presence at $k_y = \pm 3.7\ \mu m^{-1}$ of two Hamilton's diabolical points [35] (Fig. 1B). For these states, degenerate in energy, the TE-TM energy splitting exactly compensates the X-Y splitting.

It is now possible to lift the dispersion degeneracy at the two diabolical points, by applying an external magnetic field (B), perpendicular to the planar microcavity by using a peculiar property of polaritons, their excitonic component, through the Zeeman effect (Figs. 2A, B). This effect breaks the time-reversal symmetry and the polariton modes acquire a circular polarization component. By applying 9 T, the spectrum opens up at the two crossing points of the polariton dispersions, generating an anti-crossing gap (Figs. 2C, D). Here, we can extract the Zeeman strength for each couple of orthogonal modes from the photoluminescence profile of

the unpolarized energy dispersion spectra (Fig. 2B). We found that the Zeeman splitting increases at higher energies due to the higher exciton fraction of the polaritonic modes (Fig. S4B), in contrast to the TE-TM and X-Y splitting, which instead decrease moving towards the exciton energy (Fig. S4C).

In order to verify if these nontrivial dispersions are consistent with the conical diffraction theory [37], we have measured the polarization resolved photoluminescence spectra of the modes along all the six polarization axes of the Poincaré sphere, corresponding to the horizontal-vertical (H−V), diagonal-antidiagonal (D−A), and circular right-left (R−L) polarization. In particular, at the energy E = 2.313 *eV*, for which the two modes cross each other at the diabolical points, we observe that the linear polarization direction precesses when moving along the two crossing rings (dashed lines in Figs. S5 A,B), in agreement with the conical diffraction theory. At the diabolical points, the polarization value is the linear superposition of the polarizations of the crossing modes. Along the k_x direction, diametrically opposed points possess orthogonal polarization for each ring and the polarization map is centrosymmetric with respect to the origin of the momentum plane $\{k_x, k_y\} = \{0, 0\}\,\mu m^{-1}$.

The full knowledge of the mode polarization is a fundamental parameter since it defines the particle pseudospin (Stokes vector) This can be thought as a two-degree of freedom phase associated to the particles, or in other terms as a vector charge [35] property and it makes possible to extract the quantum geometric tensor (QGT) [38] (Section VI of SI). Such tensor contains the information on how the orientation of the pseudospin changes when moving along the momentum plane. The orientation of the Stokes vector **S**(**k**), which represents the polarization state as a point on the Poincaré sphere allows to reconstruct the components of the QGT and in particular the Berry curvature (Section VI SI) [14].

Note that using the effective Hamiltonian (1), QGT components can be computed analytically [38], in particular, the Berry curvature reads:

$$B_z = \pm \frac{\beta\left(\alpha\zeta \cos\varphi_\alpha \mathbf{ku}_{\pi-\zeta} - \alpha\zeta \sin\varphi_\alpha \mathbf{ku}_{\frac{\pi}{2}-\zeta} + \beta k^2\left(2\Delta_z + \zeta \mathbf{ku}_\zeta\right)\right)}{\left(\left(\beta\left(k_x^2 - k_y^2\right) + \alpha\cos\varphi_\alpha\right)^2 + \left(2\beta k_x k_y + \alpha \sin\varphi_\alpha\right)^2 + \left(\Delta + \zeta \mathbf{ku}\right)^2\right)^{3/2}} \quad (3)$$

Here, **u** are unitary vectors in the corresponding directions (e.g. $\mathbf{u}_{\frac{\pi}{2}-\zeta}$ is perpendicular to $\mathbf{u}_\zeta$). This formula shows that the variation of the parameters α, β, ζ, and Δ_z, given by the different exciton/photon fraction at each mode, allows a remarkable change of the Berry curvature

distribution in reciprocal space, that is, of the so-called band geometry, as we demonstrate experimentally below.

Fig. 3A-D shows the experimental Berry curvature distribution related to the lower energy band of the two LPBs for the modes j, j+1, j+2 split by the magnetic field (the dispersion is shown in Fig. S6A of the SI). The Berry curvature is evaluated for each state of the 2D dispersion. Fig. 3A,B shows the Berry curvature distribution for the mode *j* at 0 T and 9 T, respectively. The Berry curvature is peaked around the two anti-crossing points, forming two broadened Berry monopoles. At B=0 T this distribution is affected by the OA; in this case, instead of being zero, the circular polarization degree and Berry curvature at the two anticrossing points are of opposite sign. The integrated Berry curvature over the whole band (Chern number) is still zero, as it was the case in [32, 33]. At B=9 T (Fig. 3B), TRS is broken by the exciton Zeeman splitting, which is here much larger than the OA ($\zeta = 0.01\ meV \cdot \mu m$). The two anticrossing points of each split band have now the same sign of the circular polarization. The bands are therefore characterized by a non-zero Chern number. The exciton-photon fraction varies across different LPB pairs (values for each band doublet are reported in Table S4) and this results in different parameters which enter in the effective Hamiltonian. This completely modifies the shape of the Berry curvature distribution, as shown in the Fig. 3C-D.

The Berry curvature evolves towards a ring-like shape at higher excitonic fractions in good agreement with the simulated Berry curvatures (Fig. 3E-H), considering the experimental values of α, β, Δ_z, ζ and φ_α, extracted for each polariton mode. The evolution of the Berry curvature can therefore be understood taking into account that at higher energies the exciton fraction of the polariton modes increases, resulting in a more pronounced Zeeman splitting [38] and in a decrease of the TE-TM and X-Y splitting, due to the dispersion flattening at the exciton transition. It is the opposite trend of the contributions to the effective magnetic field with respect to the photon-exciton fraction of the polariton modes, which makes ultimately possible to observe Berry curvatures with different shapes inside the same device. Interestingly, the orientation of the linear birefringence (polarization of mode at k=0, for zero applied field) clearly depends on the exciton-photon fraction, with $\varphi_\alpha \sim 0$ for *j* and *j+1* and $\varphi_\alpha \sim 30°$ for *j+2*. This is visible in Fig. 3D,H, where the Berry curvature maxima are not along the $k_x = 0$ axis. Small discrepancies between experimental and simulated Berry curvatures can be attributed to

dissipative effects and inhomogeneity of the sample neglected in the theoretical model.

In this sample, the contribution of the OA to the Berry curvature map is crucial at 0 T, but it becomes only a small correction at 9 T. However, we observed that the OA magnitude changes from one crystal to another, proportional to the crystal thickness (Section VII of SI). It decreases in thinner samples because of a larger mode splitting, while the OA is prominent in thicker crystals, strongly affecting the Berry curvature even at 9 T (Fig. S7).

So far, we have shown how to control the parameters of the effective Hamiltonian and qualitatively modify the Berry curvature distribution by passing from one branch to another. In the next part, we demonstrate a fine control of the Berry curvature distributions and values in a given band by continuous tuning of either the magnetic field intensity, or the temperature.

In order to observe the evolution of the Berry curvature with respect to the applied magnetic field, we use in the following samples with thinner crystals (≅ 2 μm), which results in a negligibly small OA (Fig. S8). Fig. 4A shows the trend of the maximum of the Berry curvature B_0 (with the integral curvature normalized to 1) as function of the magnetic fields for 2 different polariton bands: B_0 decreases for each band by increasing the magnetic field. This parameter is fully relevant for band characterization and determines the maximal value of the anomalous Hall deviation which can be observed for a given band: $\Delta X_{AHE} \sim \sqrt{B_0}$. The experimental data (black and red points) are fitted with the eq. (S3) (black and red lines), considering 0.372 and 0.229 as photonic fractions for band 2 and band 1, respectively.

Fig. 4B shows the maximum of the Berry curvature of a polariton band versus temperature sample. When the temperature increases from 4 K to 100 K, the exciton resonance moves towards higher energy (Extended data Fig. 1A-C) resulting in a blue shift of the polariton modes. This leads to the continuous increase of the photonic fractions for each mode and a corresponding perturbation of the Berry curvature distribution (Extended data Fig. 1D-F), characterized by another quantitative parameter, the asymmetry ratio (Extended data Fig. 1G). For the band 1, reported in Extended data Fig. 1A-C, B_0 increases while increasing the photonic fraction from 0.344 at 4 K to 0.366 at 100 K.

To summarize, in Fig. 4C we show all maximum values of Berry curvature, which we have been able to measure in our samples. The points in blue correspond to the cases shown for different bands (Fig. 3 and S8), the points in red correspond to data changing the photonic

fraction on the same microcavity sample (Fig. 4). They are much closer to each other and demonstrate the possibility to finely tune the value of the Berry curvature while a coarse tuning is obtained by changing polariton bands.

Finally, we have also extracted the Berry curvature at room temperature for a $\cong 3\ \mu m$-thick crystal, despite the broadening of the polariton modes at higher temperatures (Extended data Fig. 1A). The Berry curvature at 9 T for the mode at 2280 meV is reported in Section X of the SI clearly showing two localized maxima in the reciprocal space.

II. CONCLUSIONS

Our results demonstrate that the perovskite based polariton system gives a unique opportunity to engineer the shape and value of the Berry curvature, by actively tuning different parameters, such as the crystal thickness, the applied magnetic field, and the temperature.

We have demonstrated the topological features of a 2D perovskite-based polariton system, from cryogenic to room temperature and for different band geometries. By combining the material's optical birefringence and emergent optical activity with the Zeeman effect, we have shown that perovskite-based polariton systems give a unique opportunity to engineer the shape of the Berry curvature distribution and its maximal values by actively tuning different parameters. Varying the temperature and the intensity of the external magnetic field, we actively influence the distribution of the Berry curvature, having easy access to various theoretically predicted shapes. Such kind of structures can be used for multiplexing the future optical valleytronic devices, such as transistors based on the anomalous Hall effect, operating at different wavelengths at the same time and at different temperatures.

Acknowledgments

The authors acknowledge Paolo Cazzato for technical support, Iolena Tarantini for the metal evaporation, Dario Gerace and Antonio Gianfrate for useful discussions. The authors acknowledge the project PRIN Interacting Photons in Polariton Circuits – INPhoPOL (Ministry of University and Scientific Research (MIUR), 2017P9FJBS_001), the project "TECNOMED - Tecnopolo di Nanotecnologia e Fotonica per la Medicina di Precisione", (Ministry of University

and Scientific Research (MIUR) Decreto Direttoriale n. 3449 del 4/12/2017, CUP *B*83*B*17000010001) and the “Accordo bilaterale CNR/RFBR (Russia) - triennio 2021-2023”. G.G. gratefully acknowledges the project PERSEO-PERrovskite-based Solar cells: towards high Efficiency and lOng-term stability (Bando PRIN 2015-Italian Ministry of University and Scientific Research (MIUR) Decreto Direttoriale 4 novembre 2015*n.*2488, project number 20155*LECAJ*). D.D.S and G.M. acknowledge the support of the projects EU "QUANTOPOL" (846353), "Quantum Fluids of Light" (ANR-16-CE30-0021), of the ANR Labex GaNEXT (ANR-11-LABX-0014), and of the ANR program "Investissements d'Avenir" through the IDEX-ISITE initiative 16-IDEX-0001 (CAP 20-25).

Q.X. gratefully acknowledges National Natural Science Foundation of China (No. 12020101003), strong support from the State Key Laboratory of Low-Dimensional Quantum Physics and start-up grant from Tsinghua University.

Author Contributions Statement

L.P. realized the experiments with the help of M.D.G. and G.L. D.S., G.L. and M.D.G. supervised the experimental part with the help of V.A., F.T. and D.B. L.P, L.D.M, A.C., M.P., C.T.P., Q.X., A.F. and V.M. fabricated the samples. A.M., C.G carried out the structure characterization by single-crystal X-ray diffraction and V.O. performed X-ray measurements. D.D.S., G.M., G.L., and L.D performed the treatment of the experimental data. D.D.S. and G.M. performed analytical calculations. L. P., M.D.G, L.D. with the help of G.L. and D.S. wrote the manuscript with input from all the authors. All authors have contributed to the discussion of the work.

Competing Interests Statement

The authors declare no competing interests.

Figures:

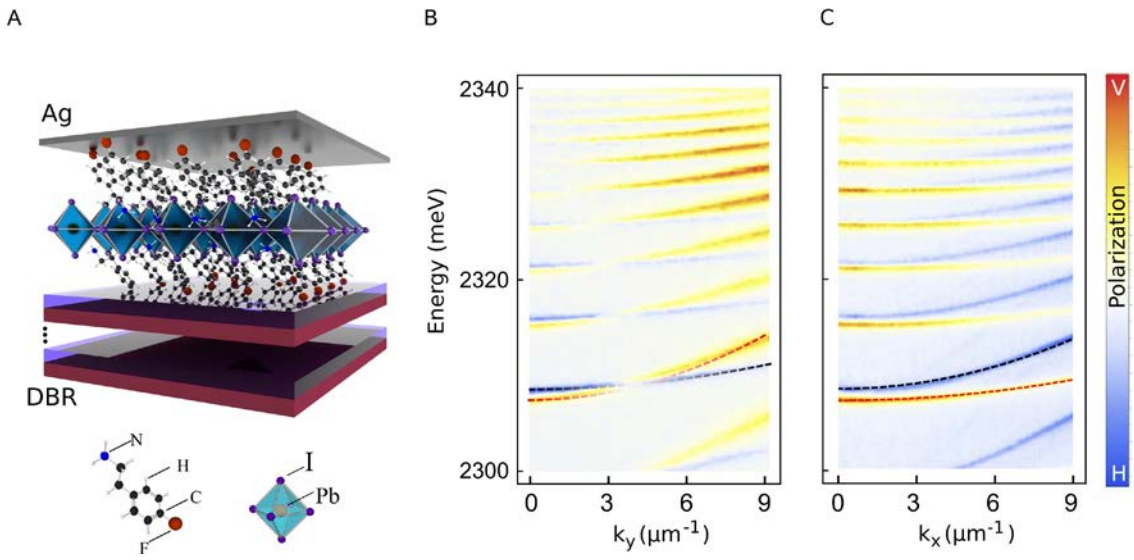

Figure 1: A) Schematic representation of a sample. Perovskite crystals are embedded in a planar microcavity made by a bottom DBR with seven TiO_2/SiO_2 pairs and a top 80 *nm* thick silver mirror. B, C) Degree of linear polarization (H/V) of the photoluminescence signal of the lower polariton branches resolved in the energy vs k_y (B) and k_x (C) in-plane momentum space. The perovskite thickness of this sample is 7 μm. The dashed lines are the fitting of the system eigenstates derived from eq. 2 with zero magnetic field (Δ_z=0) with the following parameters: E_0 = 2.308 *eV*, m = 4.4 · 10^{-4} m_e, β = 3.3 · 10^{-5} *eV μm*^{2} and α = 1.1 *meV*.

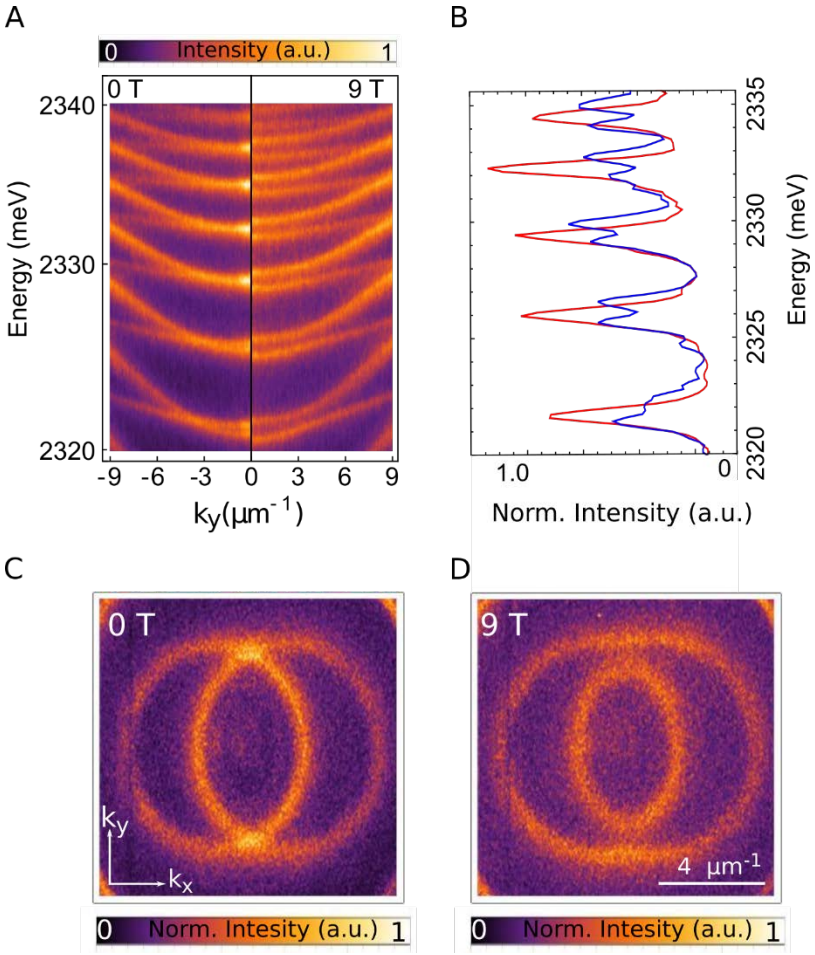

Figure 2: A) Energy vs k_y in-plane momentum of unpolarized photoluminescence for B = 0 T magnetic field (left half panel) and under an external magnetic field, B = 9 T (right half panel) measured at T = 4 K. B) Photoluminescence spectra measured at k_x = 0 μm^{-1} and k_y = ± 3.7 μm^{-1} at zero magnetic field (red line) and at B = 9 T (blue line). C, D) Unpolarized photoluminescence maps in the momentum space at isoenergetic cross-sections of the lower polariton dispersion. The cuts are taken at the energy E = 2.316 eV and for a magnetic field of B = 0 T (C) and B = 9 T (D), respectively. The Zeeman effect emerging under 9 T is responsible for the degeneracy suppression.

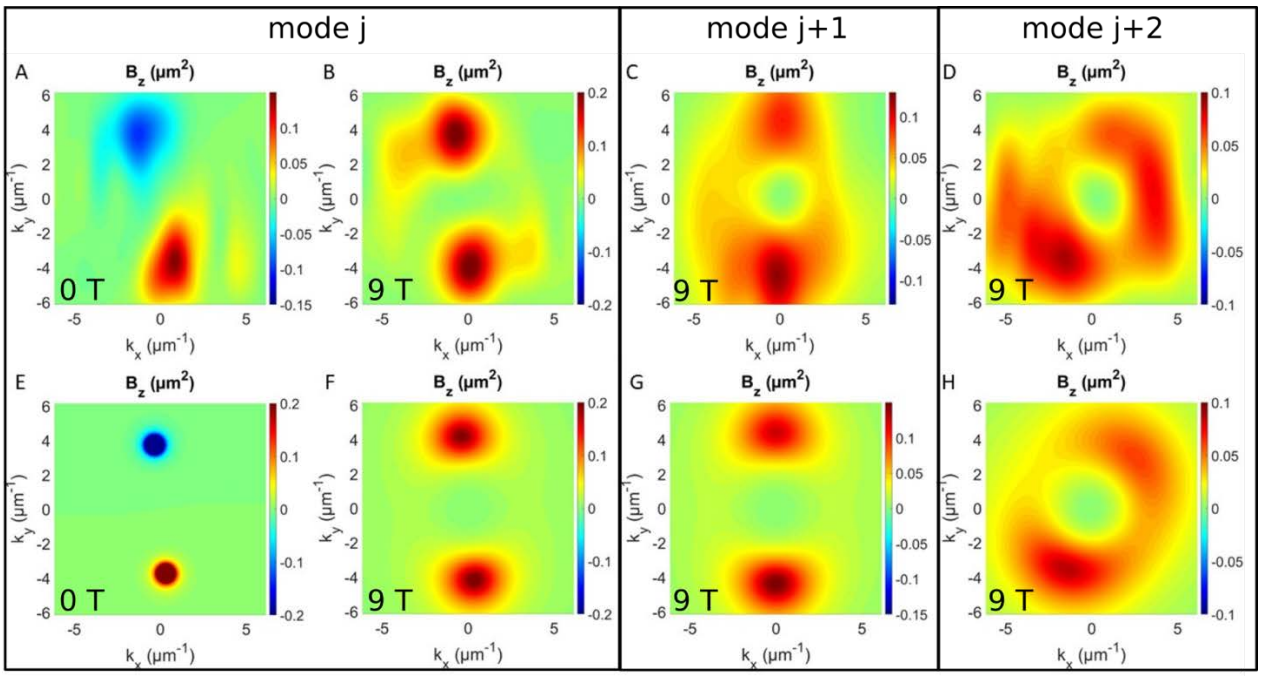

Figure 3: A-H) Experimental and theoretical Berry curvature extracted from the polarization-resolved measurements, for lower energy band (corresponding to the solution with sign + in the Eq. 3) of the mode *j* (A, E) at 0 T and (E-F) at 9 T, mode *j*+1 (C, G) and mode *j*+2 (D, H) at 9 T, respectively.

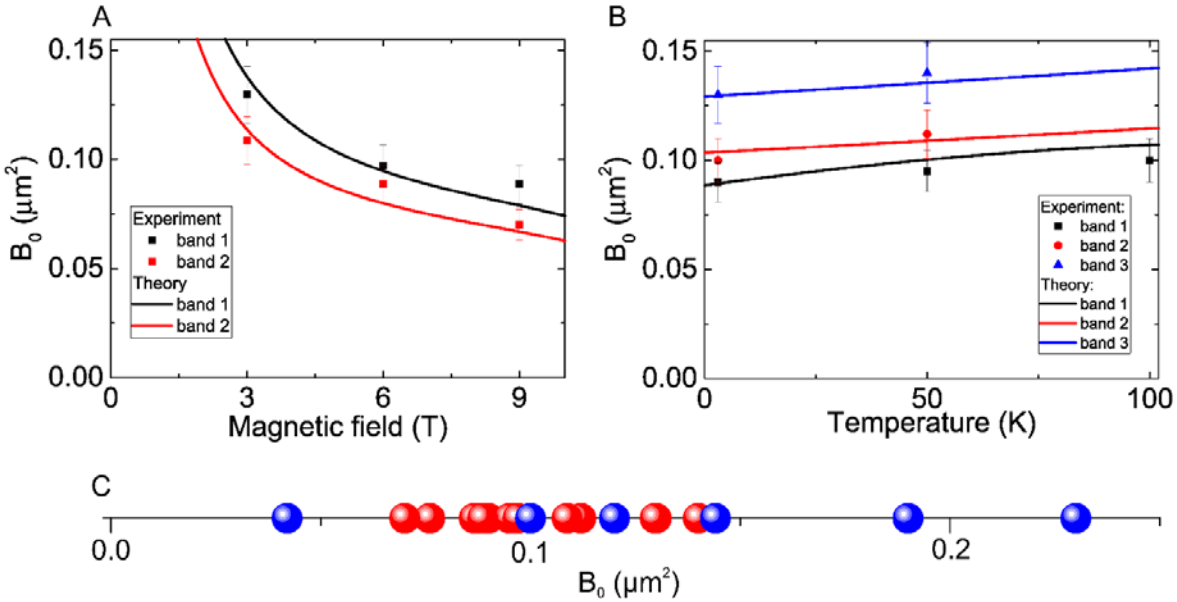

Figure 4: A) Trend of the normalized maximal Berry curvature value (B_0) as a function of the magnetic field, for band 1 and 2 reported in Fig. S8. B) Trend of the Berry curvature value as a function of the sample temperature for all polariton modes reported in Extended data Fig. 1. The error bars indicate the measurement uncertainty. C) Summary of the values extracted of the Berry curvature for all the performed experiments. Red points: measurements shown in Fig. 4, panels A and B changing the photonic fraction on the same microcavity sample. Blue points: measurements shown in Figs. 3, S8, and all other experiments reported in the manuscript for different bands, resulting in different values of the Berry curvature.

References

[1] M. Aidelsburger, S. Nascimbene, and N. Goldman, "Artificial gauge fields in materials and engineered systems," *Comptes Rendus Physique*, vol. 19, p. 394, 2018.

[2] J. Dalibard, "Introduction to the physics of artificial gauge fields," arXiv:1504.05520 [cond-mat.quant-gas], 2015.

[3] N. Goldman, J. C. Budich, and P. Zoller, "Topological quantum matter with ultracold gases in optical lattices," *Nature Physics*, vol. 12, p. 639, 2016.

[4] N. Goldman, G. Juzeliunas, P. Öhberg, and I. B. Spielman, "Light-induced gauge fields for ultracold atoms," *Reports on Progress in Physics*, vol. 77, p. 126401, 2014.

[5] L. Lu, J. D. Joannopoulos, and M. Soljacic, "Topological photonics," *Nature Photonics*, vol. 8, p. 821, 2014.

[6] M. Hafezi, "Synthetic gauge fields with photons," *International Journal of Modern Physics B*, vol. 28, p. 1441002, 2014.

[7] T. Ozawa, H. M. Price, A. Amo, N. Goldman, M. Hafezi, L. Lu, M. C. Rechtsman, D. Schuster, J. Simon, O. Zilberberg *et al.*, "Topological photonics," *Reviews of Modern Physics*, vol. 91, p. 015006, 2019.

[8] M. A. Vozmediano, M. Katsnelson, and F. Guinea, "Gauge fields in graphene," *Physics Reports*, vol. 496, p. 109, 2010.

[9] Y. Ren, Z. Qiao, and Q. Niu, "Topological phases in two-dimensional materials: a review," *Reports on Progress in Physics*, vol. 79, p. 066501, 2016.

[10] S. D. Huber, "Topological mechanics," *Nature Physics*, vol. 12, p. 621, 2016.

[11] T. Gao, E. Estrecho, K. Bliokh, T. Liew, M. Fraser, S. Brodbeck, M. Kamp, C. Schneider, S. Höfling, Y. Yamamoto *et al.*, "Observation of non-hermitian degeneracies in a chaotic exciton-polariton billiard," *Nature*, vol. 526, p. 554, 2015.

[12] E. Estrecho, T. Gao, S. Brodbeck, M. Kamp, C. Schneider, S. Höfling, A. Truscott, and E. Ostrovskaya, “Visualising berry phase and diabolical points in a quantum exciton-polariton billiard,” *Scientific reports*, vol. 6, p. 37653, 2016.

[13] H.-T. Lim, E. Togan, M. Kroner, J. Miguel-Sanchez, and A. Imamoglu, “Electrically tunable artificial gauge potential for polaritons,” *Nature communications*, vol. 8, p. 14540, 2017.

[14] A. Gianfrate, O. Bleu, L. Dominici, V. Ardizzone, M. De Giorgi, D. Ballarini, G. Lerario, K. W. West, L. N. Pfeiffer, D. D. Solnyshkov, D. Sanvitto, and G. Malpuech, “Measurement of the quantum geometric tensor and of the anomalous Hall drift,” *Nature*, vol. 578, p. 7795, 2020.

[15] S. Raghu and F. D. Haldane, “Analogs of quantum-Hall-effect edge states in photonic crystals,” *Physical Review A - Atomic, Molecular, and Optical Physics*, vol. 78, p.033834, 2008.

[16] T. Karzig, C. E. Bardyn, N. H. Lindner, and G. Refael, “Topological polaritons”, *Physical Review X*, vol. 5, p. 031001, 2015.

[17] A. Kavokin, G. Malpuech, and M. Glazov, “Optical spin hall effect,” *Physical Review Letters*, vol. 95, p. 135501, 2005.

[18] C. E. Bardyn, T. Karzig, G. Refael, and T. C. Liew, “Topological polaritons and excitons in garden-variety systems,” *Physical Review B - Condensed Matter and Materials Physics*, vol. 91, p. 161413, 2015.

[19] A. V. Nalitov, D. D. Solnyshkov, and G. Malpuech, “Polariton Z topological insulator,” *Physical Review Letters*, vol. 114, p. 116401, 2015.

[20] S. Klembt, T. H. Harder, O. A. Egorov, K. Winkler, R. Ge, M. A. Bandres, M. Emmerling, L. Worschech, T. C. Liew, M. Segev, C. Schneider, and S. Höfling, “Exciton-polariton topological insulator,” *Nature*, vol. 112, p. 552, 2018.

[21] T. Jacqmin, I. Carusotto, I. Sagnes, M. Abbarchi, D. D. Solnyshkov, G. Malpuech, E. Galopin, A. Lemaître, J. Bloch, and A. Amo, “Direct observation of Dirac cones and a flatband in a honeycomb lattice for polaritons,” *Physical Review Letters*, vol. 112, p. 116402, 2014.

[22] B. Real, O. Jamadi, M. Milicévic, N. Pernet, P. St-Jean, G. Ozawa, I. Montambaux, I. Sagnes, A. Lemaître, L. Le Gratiet, A. Harouri, S. Ravets, J. Bloch, and A. Amo, “Semi-Dirac transport and

anisotropic localization in polariton honeycomb lattices," *arXiv*: 2004.03478 *[cond-mat.mes-hall]*, 2020.

[23] M. Milicévic, T. Ozawa, G. Montambaux, I. Carusotto, E. Galopin, A. Lemaître, L. Le Gratiet, I. Sagnes, J. Bloch, and A. Amo, "Orbital Edge States in a Photonic Honeycomb Lattice," *Physical Review Letters*, vol. 118, p. 107403, 2017.

[24] F. Scafirimuto, D. Urbonas, U. Scherf, R. F. Mahrt, and T. Stöferle, "Room-Temperature Exciton-Polariton Condensation in a Tunable Zero-Dimensional Microcavity," *ACS Photonics*, vol. 5, p. 85, 2018.

[25] R. Su, S. Ghosh, J. Wang, S. Liu, C. Diederichs, T. C. Liew, and Q. Xiong, "Observation of exciton polariton condensation in a perovskite lattice at room temperature," vol. 16, p. 301, 2020.

[26] L. Pedesseau, D. Sapori, B. Traore, R. Robles, H. H. Fang, M. A. Loi, H. Tsai, W. Nie, J. C. Blancon, A. Neukirch, S. Tretiak, A. D. Mohite, C. Katan, J. Even, and M. Kepenekian, "Advances and Promises of Layered Halide Hybrid Perovskite Semiconductors," vol. 10, p. 9776, 2016.

[27] B. Saparov and D. B. Mitzi, "Organic-Inorganic Perovskites: Structural Versatility for Functional Materials Design", Chem. Rev., vol.10, p. 4558, 2016.

[28] F. Thouin, S. Neutzner, D. Cortecchia, V. A. Dragomir, C. Soci, T. Salim, Y. M. Lam, R. Leonelli, A. Petrozza, A. R. S. Kandada, and C. Silva, "Stable biexcitons in two-dimensional metal-halide perovskites with strong dynamic lattice disorder," *Physical Review Materials*, vol. 2, p. 034001,2018.

[29] L. Polimeno, A. Fieramosca, G. Lerario, M. Cinquino, M. De Giorgi, D. Ballarini, F. Todisco, L. Dominici, V. Ardizzone, M. Pugliese, C. T. Prontera, V. Maiorano, G. Gigli, L. De Marco, and D. Sanvitto, "Observation of Two Thresholds Leading to Polariton Condensation in 2D Hybrid Perovskites," *Advanced Optical Materials*, vol. 8, p. 2000176, 2020.

[30] A. Fieramosca, L. Polimeno, V. Ardizzone, L. De Marco, M. Pugliese, V. Maiorano, M. De Giorgi, L. Dominici, G. Gigli, D. Gerace *et al.*, "Two-dimensional hybrid perovskites sustaining strong polariton interactions at room temperature," *Science advances*, vol. 5, p. 9967, 2019.

[31] A. Fieramosca, L. De Marco, M. Passoni, L. Polimeno, A. Rizzo, B. L. Rosa, G. Cruciani, L. Dominici, M. De Giorgi, G. Gigli *et al.*, "Tunable out-of-plane excitons in 2d single-crystal perovskites," *ACS Photonics*, vol. 5, p. 4179, 2018.

[32] K. Rechcinska, M. Król, R. Mazur, P. Morawiak, R. Mirek, K. empicka, W. Bardyszewski, M. Matuszewski, P. Kula, W. Piecek, P. G. Lagoudakis, B. Pietka, and J. Szczytko, "Engineering spin-orbit synthetic Hamiltonians in liquid-crystal optical cavities," *Science*, vol. 366, p. 727, 2019.

[33] J. Ren, Q. Liao, F. Li, Y. Li, O. Bleu, G. Malpuech, J. Yao, H. Fu, and D. Solnyshkov, "Nontrivial band geometry in an optically active system," *arXiv:1912.05994 [cond-mat]*, 2019.

[34] F. Lédée, G. Trippé-Allard, H. Diab, P. Audebert, D. Garrot, J.-S. Lauret, and E. Deleporte, "Fast growth of monocrystalline thin films of 2d layered hybrid perovskite," *CrystEngComm*, vol. 19, p. 2598, 2017.

[35] A. Fieramosca, L. Polimeno, G. Lerario, L. De Marco, M. De Giorgi, D. Ballarini, L. Dominici, V. Ardizzone, M. Pugliese, V. Maiorano, G. Gigli, C. Leblanc, G. Malpuech, D. Solnyshkov, and D. Sanvitto, "Chromodynamics of photons in an artificial non-Abelian magnetic Yang-Mills field," *arXiv*: 1912.09684 *[cond-mat],* 2019.

[36] S. Donati, L. Dominici, G. Dagvadorj, D. Ballarini, M. De Giorgi, A. Bramati, G. Gigli, Y. G. Rubo, M. H. Szymanska, and D. Sanvitto, "Twist of generalized skyrmions and spin vortices in a polariton superfluid," *Proc. Natl. Acad. Sci.*, vol. 113, p. 14926, 2016.

[37] M. V. Berry and M. R. Dennis, "The optical singularities of birefringent dichroic chiral crystals," *Proceedings of the Royal Society A: Mathematical, Physical and Engineering Sciences*, vol. 459, p. 1261, 2003.

[38] O. Bleu, D. D. Solnyshkov, and G. Malpuech, "Measuring the quantum geometric tensor in two-dimensional photonic and exciton-polariton systems," *Phys. Rev. B*, vol. 97, p. 195422, 2018.

[47] S. Waltersperger, V. Olivier, C. Pradervand, W. Glettig, M. Salathe, M. R. Fuchs, A. Curtin, X. Wang, S. Ebner, E. Panepucci, T. Weinert, C. Schulze-Briese, M. Wang, "PRIGo: a new multi-axis goniometer for macromolecular crystallography", *J. Synchrotron Rad.*, vol. 22, p. 895, 2015.

[48] W. Kabsch, "*XDS*", *Acta Cryst. D*, vol. 66, p. 125, 2010.

[49] C. Giacovazzo, Phasing in Crystallography: A Modern Perspective, *Oxford University Press*, 2014.

[50] M. C. Burla, R. Caliandro, B. Carrozzini, G. L. Cascarano, C. Cuocci, C. Giacovazzo, M. Mallamo, A. Mazzone, G. Polidori, "Crystal structure determination and refinement *via SIR2014*", *J. Appl. Cryst.*, vol. 48, p. 306, 2015.

[51] G. M. Sheldrick, "*SHELXT*- Integrated space-group and crystal-structure determination", *Acta Cryst. A*, vol. 71, p. 3, 2015.

METHODS

Synthesis of 2*D* perovskite flakes

A solution 0.5 M PEAI-F is prepared in a nitrogen- filled glovebox by dissolving PbI_2 and 4-Fluorophenethylammonium iodide (1:2 molar ratio) in *γ*-butyrolactone and stirring at 70°*C* for 1 hour. 2D perovskite single crystals are synthesized using an anti-solvent vapor-assisted crystallization method as follows: 3 μl of perovskite solution are deposited on top a sputtered DBR and covered with a glass coverslip. Substrates and a small vial containing 2 ml of dichlorometane are placed inside a bigger Teflon vial which is closed with a screw cap and left undisturbed for 12 hours at room temperature. During this time, crystals slowly grow in a saturated environment of dichloromethane (antisolvent) and at the end millimeter-sized perovskite flakes appear on the top of the DBR. Their thickness varies from few to tens of micrometers. Using SPV 224PR-M Nitto Tape or PDMS, mechanical exfoliation is carried out on the perovskite flakes in order to obtain single crystals having the desired thickness.

Microcavity Sample Fabrication

The DBR is made by seven pairs of TiO_2/SiO_2 (63 *nm*/94 *nm*) deposited by radio-frequency (RF) sputtering process— in an Argon atmosphere under a total pressure of $6 \cdot 10^3$ mbar and at RF power of 250 *W* —on top of a 1 *mm* glass substrate. The perovskite single crystals are grown on top of the DBR (see above) and an 80 nm-thick layer of silver is thermally evaporated on top of the structure (deposition parameters: current = 280 *A*, deposition-rate = 3 Å/*s*).

X-ray diffraction

Single-crystal X-ray diffraction data measurements for PEAI-F were carried out at the beamline PXIII (X06DA-PXIII, http://www.psi.ch/sls/pxiii/) at the Swiss Light Source (SLS), Villigen, Switzerland, using a Parallel Robotics Inspired (PRIGo) multiaxis goniometer [47] and a PILATUS 2M-F detector. Data collection was performed at low temperature (T = 100 K) on a selected crystal

mounted on litholoops (Molecular Dimensions). Complete data were obtained by merging two 360° ω scans at χ=0° and χ=30° of PRIGo. In shutterless mode, a 360° data set was collected in 3 min (beam energy of 17 keV, λ=0.72932 Å, focus size 90 x 50 μm^2, 0.25 sec of exposure time per frame, 0.5° scan angle). Main experimental details are given in Table S1. Diffraction data were processed by *XDS* [48], a software organized in eight subroutines able to perform the main data reduction steps; the integrated intensities were scaled and corrected for absorption effects by the *XSCALE* subroutine [48].

Structure solution was carried out by Direct Methods [49] using *SIR2019* [50] a package that exploits the information on unit cell parameters, diffraction intensities and expected chemical formula to identify the space group and determine the crystal structure by Direct Methods. The partial structure model located by *SIR2019* was completed and refined using full-matrix least-squares techniques by *SHELXL2014/7* [51]. Non-hydrogen atoms were refined anisotropically. Hydrogen atoms were positioned by difference Fourier map; their atomic coordinates were freely refined and the following constraints on the isotropic U value of H atoms were applied: U_{iso}(H)=1.2 U_{eq}(C) and U_{iso}(H)=1.5 U_{eq}(N) in case of hydrogen atoms bonded to C and N atoms, respectively.

Optical setup

The samples were inserted in a cryostat equipped with a resistor to control the operation temperature and cooled down to liquid helium for high magnetic field measurements. Extended Data Fig. 2 shows a sketch of the optical setup. The measurements are performed in reflection configuration, using a closed-cycle attoDRY1000 cryostation, a continuous- wave laser at 488 *nm* (2541 meV) and an optical chopper (with rotation frequency = 300 *Hz*), to minimize the sample heating. Through the detection path, the image on the back focal plane of the detection objective (50 x with N.A. = 0.82) is projected on a spectrometer entrance slit. The spectrometer is coupled to an enhanced CCD camera for the detection of the polariton energy dispersion. The second 30cm lens is on a translation stage in order to scan the whole 2D-momentum space. The quarter-wave plate (QWP) and the half-wave plate (HWP) in front of the entrance of the spectrometer allow for the detection of the polarization-resolved maps in momentum space.

Data availability

The datasets generated and analysed during the current study are available in the Open Science Framework (OSF) repository via the following link:

https://osf.io/x5h7v/?view_only=6a9fa8e1568343f797ec5a76d4626fe1